Correlation of satellite image time-series for the detection and monitoring of slow-moving landslides

André Stumpf [a,b,c,*], Jean-Philippe Malet [a], Christophe Delacourt [c]

[a] Institut de Physique du Globe de Strasbourg, CNRS UMR 7516, EOST/Université de Strasbourg, 5 rue Descartes, Strasbourg F-67084, France
[b] Laboratoire Image Ville Environnement, CNRS UMR 7362, Université de Strasbourg, 3 rue de l'Argonne, Strasbourg F-67083, France
[c] Laboratoire Domaines Océaniques, CNRS UMR 6538, IUEM/Université de Bretagne Occidentale, Rue Dumont d'Urville, Plouzané F-29280, France

A B S T R A C T

Slow-moving landslides are widespread in many landscapes with significant impacts on the topographic relief, sediment transfer and human settlements. Their area-wide mapping and monitoring in mountainous terrain, however, is still challenging. The growing archives of optical remote sensing images offer great potential for the operational detection and monitoring of surface motion in such areas. This study proposes a multiple pairwise image correlation (MPIC) technique to obtain a series of redundant horizontal displacement fields, and different multi-temporal indicators for a more accurate detection and quantification of surface displacement. The technique is developed and tested on a series of monoscopic and stereoscopic Pléiades satellite images at a test site in the South French Alps. Empirical tests confirm that MPIC significantly increased detection accuracy ($F-measure = 0.85$) and that the measurement error can be reduced by averaging velocities from all pair combinations covering a given time-step (i.e. when stereo-pairs are available for at least one date). The derived inventory and displacement fields of 169 slow-moving landslides show a positive relationship between the landslide size and velocities, as well as a seasonal acceleration of the largest landslides in response to an increase in effective precipitation. The processing technique can be adapted to better exploit increasingly available time-series from a variety of optical satellites for the detection and monitoring of landslide displacement.

© 2016 Elsevier Inc. All rights reserved.

1. Introduction

Landslides constitute a major natural hazard and a dominant geomorphic agent in many mountainous landscapes with diverse impacts on topographic relief, sediment transport and human settlements. Rapid slope failures triggered by earthquakes and rain storms account for the vast majority of related casualties (Petley, 2012) but also continuously active, slow-moving landslides are a widespread phenomenon causing severe damages to infrastructure and alterations of the sediment budget (Mackey and Roering, 2011; Mansour et al., 2011). Landslide inventory maps are, therefore, fundamental for the quantification of sediment budgets and natural hazards but their elaboration through field work and visual image interpretation often remains a tedious task (Guzzetti et al., 2012).

Consequently, considerable research efforts have already been dedicated to the development of more automated remote sensing techniques for landslide inventory mapping. Studies on the analysis of optical satellite data, focus predominantly on the mapping of rapid landslides which typically lead to a removal of the vegetation cover in post-failure state (e.g. Behling et al., 2016, 2014; Joyce et al., 2009; Kurtz et al., 2014; Li et al., 2016; Lu et al., 2011; Martha et al., 2010, 2012; Mondini et al., 2011; Stumpf and Kerle, 2011; Stumpf et al., 2014a). For the detection and monitoring of very slow and extremely slow landslides (Cruden and Varnes, 1996), in contrast, Interferometric Synthetic Aperture Radar (InSAR) has proven to be particularly suitable (e.g. Handwerger et al., 2013; Lauknes et al., 2010; Zhao et al., 2012). The use of InSAR is typically limited to landslides slower than $1.0 \, \text{m} \cdot \text{yr}^{-1}$, on slopes without dense vegetation cover, with favorable slope exposition, and with significant displacement along the line-of-sight of the satellite (Wasowski and Bovenga, 2014). The detection and frequent monitoring of slow-moving landslides with such techniques remains challenging (Schlögel et al., 2015a).

Template-based matching of optical remote sensing images is used frequently to measure surface displacement related to geomorphological and tectonic processes at sub-pixel precision (Leprince et al., 2008; Stumpf et al., 2016, and references therein). Despite the sub-pixel precision of available image correlation algorithms (e.g. Debella-Gilo and Kääb, 2011; Leprince et al., 2007; Rosu et al., 2015),

* Corresponding author at: Laboratoire Image Ville Environnement, CNRS UMR 7362, Université de Strasbourg, 3 rue de l'Argonne, Strasbourg F-67083, France.

a number of potential error sources still often lead to false detections or biased measurements. Limitations can arise from imperfect sensor models, co-registration and orthorectification residuals linked to the DSM (Digital Surface Model) errors, but also from the study site characteristics such as the presence of a dense vegetation cover, cast shadows, low contrast areas or apparent movement caused by specular reflectance features and strong soil surface state changes (Stumpf et al., 2014b). Such factors often impact the accuracy of the calculated displacement fields and impose the need for careful post-processing to correct for geometric errors, outliers and noise.

Proposed techniques for the correction of geometric errors include for example destriping to correct for orbital and sensor errors (Leprince et al., 2007), and the modeling of systematic DSM errors (Scherler et al., 2008). Calibration techniques used for the latest generation of optical satellites can compensate for sensor misalignments and orbital jitter (Lebegue et al., 2012). However, non-systematic DSM errors and decorrelation due to changes in the surface aspect remain critical issues, especially for the orthorectification of very-high spatial resolution (VHSR) images acquired at variable incidence angles. Post-processing thus frequently includes masking based on the correlation coefficient (Berthier et al., 2005) or signal-noise-ratio (Scherler et al., 2008), and the application of low-pass denoising filters to filter out false matches (Heid and Kääb, 2012; Stumpf et al., 2014b). For gravitational processes such as landslides and glaciers, filters related to the direction and maximum velocity of the motion have also proven useful to remove outliers (Kääb, 2005; Scherler et al., 2008; Stumpf et al., 2014b). For surfaces with dense vegetation cover such filters can be complemented by vegetation masks obtained from multi-spectral images (Stumpf et al., 2014b) which, however, incur the possibility of not detecting surface motion in vegetated areas.

The constantly growing archives of optical remote sensing images (e.g. Landsat, SPOT-Satellite Pour l'Observation de la Terre, ALOS-Advanced Land Observation Satellite, Sentinel-2) bear a great potential to study seasonal and long-term patterns of surface motion with image correlation techniques. Given the above-mentioned limitations, however, image correlation is currently mainly suitable for the quantification of surface displacements which are coherent over large areas (e.g. coseismic slip), localized in flat terrain (e.g. dune migration) or in areas with little vegetation cover (e.g. alpine glaciers). While SAR interferometry time-series processing methods have been developed for two decades to better deal with coherence loss and atmospheric noise (Hooper et al., 2012), the fusion of time series from optical data has only recently been demonstrated to improve the coverage and accuracy of glacier flow estimates over large areas (Dehecq et al., 2015; Fahnestock et al., 2016; Rosenau et al., 2015). Applications to landslides have focused mainly on the investigation of known active landslides (Casson et al., 2005; Delacourt et al., 2004; Leprince et al., 2008; Stumpf et al., 2014b; Yamaguchi et al., 2003). Lacroix et al. (2015) demonstrated the potential of optical image correlation for the detection and quantification of landslide activations due to seismic shaking, whereas comprehensive automatic methods for the analysis of optical Satellite Image Time Series (SITS) are, to the best of our knowledge, still lacking. The usefulness of image correlation as a reliable tool for the detection and monitoring of slow-moving landslides, which can remain inactive for several years or develop on previously stable slopes, remains limited by numerous false detections.

To fill this gap, the objective of this work is to propose and test several approaches for the exploitation of optical SITS in order to improve the measurement accuracy and reduce false detections. They are based on the hypothesis that landslides feature a displacement which is more coherent in space and time than residuals resulting from imperfect co-registration, orthorectification and false matches. The technique takes advantage of multiple-pairwise image matching (MPIC) to increase the redundancy of the measurements

and exploits the resulting stack of displacement fields to quantify the displacement coherence over time. The effectiveness of several multi-temporal indicators and the accuracy of the resulting velocity fields is assessed in the Ubaye valley (South French Alps) with a multi-temporal dataset of Pléiades satellite images.

The paper is structured as follows. Section 2 introduces a multiple-pairwise image correlation scheme and the techniques to jointly analyze the resulting stack of velocity fields. The section also describes the study site along with the analyzed datasets, and the experimental protocol for assessing the sensitivity and accuracy of the proposed processing techniques. Section 3 presents the results of the sensitivity analysis, provides a discussion of the accuracy and limitations of the best performing technique, and gives an interpretation of relationships between landslide kinematics and variations of the seasonal precipitation. Finally conclusions are drawn in Section 4.

2. Methods and data

2.1. Multiple-pairwise image correlation

The processing strategy (Fig. 1) is based on the image correlation algorithm implemented in the MicMac open-source library (Pierrot-Deseilligny et al., 2015; Rosu et al., 2015). It enables parallel processing and is employed for batch-processing on High-Performance Computing (HPC) infrastructure. The algorithm follows a hierarchical matching scheme using normalized cross-correlation (NCC) with a non-linear cost function and spatial regularization to eliminate outliers. Sub-pixel resolution is achieved through step-wise interpolation of the input images which is computationally expensive but also more precise than interpolation of the correlation surface or peak-fitting methods (Debella-Gilo and Kääb, 2011). NCC-based correlation is better adapted for the use of smaller matching windows targeting small landscape features (Heid and Kääb, 2012). The proposed analysis technique, however, does not depend on a particular correlation algorithm and can be easily extended using other image correlation algorithms (e.g. Heid and Kääb, 2012; Leprince et al., 2007) for pairwise matching. The MicMac correlator has a number of parameters which can be adapted to the particular application. This comprises the size of the template window ω and the sub-pixel resolution as a parameter to negotiate between sub-pixel precision and computational runtime. The matching cost function is evaluated from the normalized cross-correlation coefficient taking into account only correlation coefficients $C \geq C_{\min}$. The exponent γ can be used to increase the relative influence of high correlation values (Rosu et al., 2015). The most likely match for each pixel is determined considering the cost-function at the pixel and the gradient to the displacement of neighboring pixels along a defined number of scan directions n_{dir}. The influence of the gradient can be adapted with a regularization parameter reg and enforces a spatial smoothness on the displacement field which allows to reduce noise and outliers. The settings used in this study are summarized in Table 1. For ω, n_{dir}, reg the default values of the implementation were used. The threshold parameter $C_{\min}$ was set to 0.3 to account for typically stronger surface changes of landslides with respect to the default value of 0.5 targeting in particular measurements of co-seismic slip (Rosu et al., 2015). The sub-pixel resolution was decreased from its default of 0.05 pixel to 0.1 pixel to reduce the computational costs.

Given a sequence of orthorectified and co-registered monoscopic images and stereo-pairs acquired at n different dates over the same area, a possible strategy is the correlation among only the multi-temporal pairs with the smallest spatial baselines to minimize the differences in incidence angles and the influence of DSM errors. This leads to a sequence of $m = n - 1$ measurements or $m = \sum_{i=1}^{t}(n - i)$ if the matching is not only performed sequentially but over a range of t subsequent dates. If the sequence includes multiple images per date, (e.g. stereo-pairs) each date can be denoted as a tuple of the
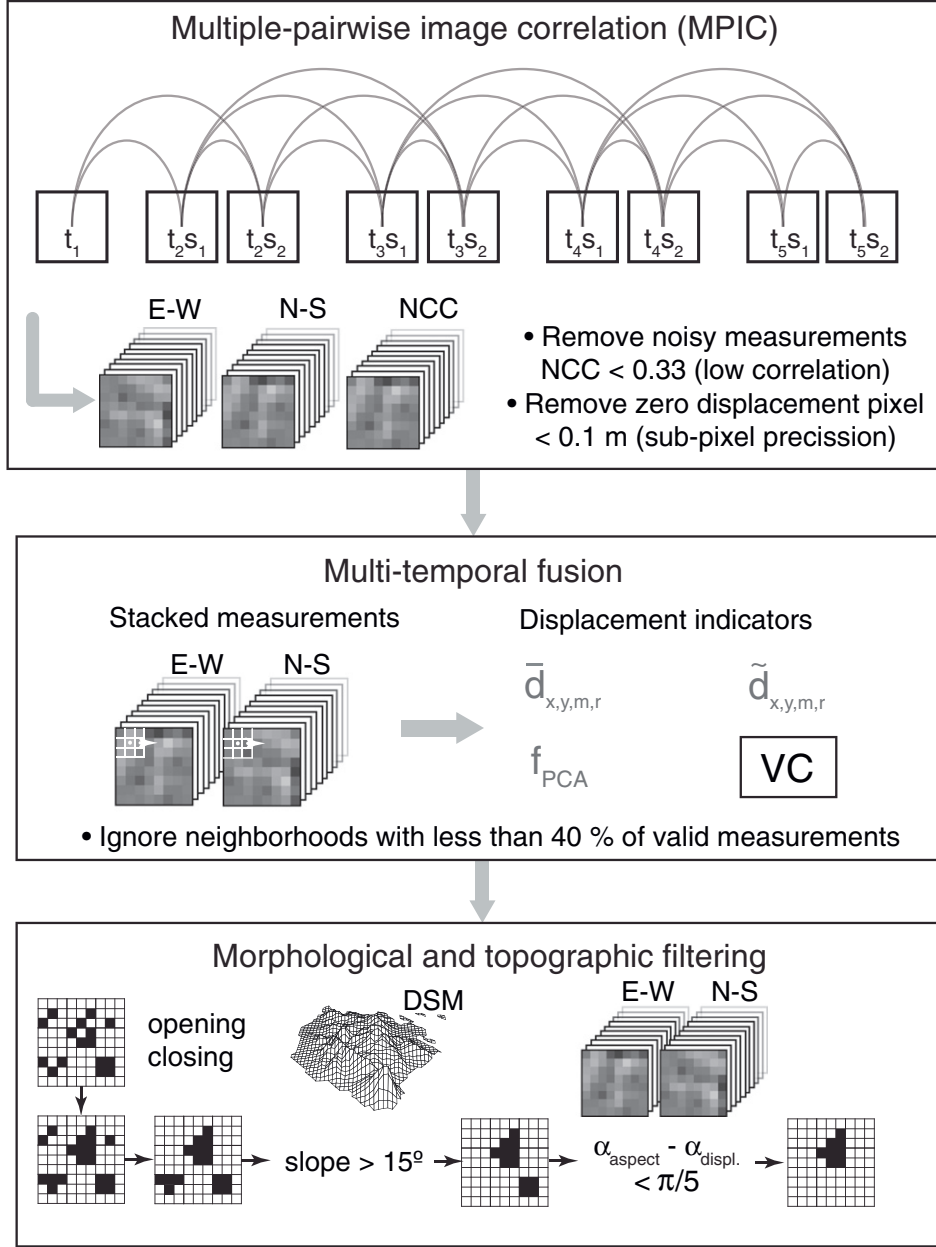
Fig. 1. Flowchart illustrating the overall processing strategy comprising multiple-pairwise image correlation among images from multiple time steps t_i and stereo-pairs s_i (Section 2.1), the comparison of four different multi-temporal indicators with the vector coherence VC being the most effective (Section 2.2), and morphological and topographic filtering (Section 2.3).

form $K = \{k_1, k_2, \ldots k_n\}$ (e.g. $k_i = 1 \rightarrow$ monoscopic, $k_i = 2 \rightarrow$ stereoscopic, etc.). Considering the number of images k_i acquired at the ith date and the simple case of $t = 1$, the number of possible combinations can be denoted as in Eq. (1).

$$m = k_1 - 1 + \sum_{i=1}^{n} k_i(k_{i+1}) + k_{i+1} - 1 \qquad (1)$$

Note that this formulation implies that matching is also performed among orthoimages of stereo-pairs of the same date ($k_1 - 1, k_{i+1} - 1$). This approach was tested with the intention to measure false positive displacements among stereo-pairs resulting from orthorectification

errors, and analyze if their inclusion in the indicators (Section 2.2) reduces spurious detections. For each pixel, the MPIC scheme yields a total of m displacement measurements constituted by two components of the horizontal displacement Δx and Δy and the correlation coefficient C. They assemble the respective image stacks denoted as $I_{\Delta x}$, $I_{\Delta y}$ and I_C. Before any further processing, stable terrain and decorrelated areas can be removed directly at this stage. For each pixel the mean displacement magnitude $\bar{d}$ over the entire stack can be computed as in Eq. (2) where $\|\|$ denotes the Euclidean norm.

$$\bar{d} = \left\| \left(\frac{1}{m} \sum_{j=1}^{m} \Delta x_j \right), \left(\frac{1}{m} \sum_{j=1}^{m} \Delta y_j \right) \right\| \qquad (2)$$

Table 1
Parameter settings for the image correlation.

Parameter	Value
ω	9
Sub-pixel resolution	0.1
C_{min}	0.3
n_{dir}	14
reg	0.2

A threshold t_C is defined so that all measurements in a given stack layer with $C \le t_C$ are flagged as missing data for the computation of the multi-temporal indicators (Section 2.2). The threshold can be adapted according to the specific application and study site, and is set to 0.33 according to a preliminary analysis of the detection accuracy with respect to changes t_C on the *validation areas* (Supplementary Data, Fig. S2a). Based on this analysis approximately $\frac{1}{3}$ of the measurements are rejected. Considering the uncertainty of the measurements, which depends on the input data and the sub-pixel precision of the matching, a threshold $t_{\tilde{d}} = 0.1$ m is defined so that all pixels with $\bar{d} \le t_{\tilde{d}}$ are flagged as stable and excluded from the analysis. Unlike for t_C this operation masks out pixels over the entire stack. This permits to eliminate numerous noisy measurements with a mean close to zero (Supplementary Data, Fig. S2c), whereas with longer time series $t_{\tilde{d}}$ should be used conservatively to avoid masking of small one-time displacements.

2.2. Multi-temporal fusion

In order to formulate meaningful indicators that enable to summarize the information in the stack of m displacement fields, it is useful to consider some physical properties of mass movements.

- coherent displacement direction over time: By definition the displacement will follow the force of gravity and is therefore very likely to maintain the same direction.
- strong correlation of spatially close displacement vectors: The rheology (e.g. cohesion, internal friction and viscosity) of the moving mass typically leads to a spatially smooth motion field.
- temporal variability of the displacement rates: Mass movements such as glaciers and landslides are controlled by changes of the material properties and external forcing factors leading to phases of acceleration and deceleration (Lacroix et al., 2015; Malet et al., 2005a; Quincey et al., 2011).

Based on those hypotheses, four indicators for the detection of persistent surface displacements are proposed. The collection of m displacement measurements for an image position (x, y) and neighboring pixels with the coordinates $x - r \le x \le x + r$ and $y - r$ to $y + r$ components Δx and Δy can be denoted by the vectors $\Delta X(x, y, m, r)$ and $\Delta Y(x, y, m, r)$, respectively, where r controls the size of the considered neighborhood. For convenience, those vectors are, denoted as ΔX and ΔY. To avoid unreliable estimates in areas where due to the applied thresholds t_C and $\tilde{d}$ relatively few measurements are available, the computed indicator value is considered valid only if at least 40% of measurements in the spatio-temporal neighborhood defined by (x, y, m, r) are valid and otherwise set to zero. The respective threshold parameter $t_m = 0.4$ was determined according to a preliminary analysis of the detection accuracy with respect to changes t_m on the *validation areas* (Supplementary Data, Fig. S2b).

2.2.1. Spatio-temporal mean

The most straightforward way to summarize a series of uncertain measurements is the use of the arithmetic mean. Extending the formulation in Eq. (2), the mean spatio-temporal displacement $(\bar{d}_{x,y,m,r})$ in the neighborhood of a given pixel can be computed as in Eq. (3) where || denotes the cardinality of the set of measurements.

$$\bar{d}_{x,y,m,r} = \left\| \left(\frac{1}{|\Delta X|} \sum_{i=1}^{|\Delta X|} \Delta X_i \right), \left(\frac{1}{|\Delta X|} \sum_{i=1}^{|\Delta Y|} \Delta Y_i \right) \right\| \quad (3)$$

2.2.2. Spatio-temporal median

While the arithmetic mean is an unbiased estimator of the expected value if the underlying distribution is normal, it is susceptible to outliers. Furthermore, it tends to blur edges in areas with strong displacement gradients as for example at the limits between the moving mass and the stable terrain. Studies on the satellite-based derivation of glacier flow velocities, therefore, often favor the median (e.g. Dehecq et al., 2015) as a more robust summary statistic. From the obtained measurements, the spatio-temporal median displacement $(\tilde{d}_{x,y,m,r})$ can be computed as denoted in Eq. (4).

$$\tilde{d}_{x,y,m,r} = \| med(\Delta X_i), med(\Delta Y_i) \| \quad (4)$$

Some examples of the variations of the proposed statistics are given in Fig. 2. Compared to the mean, the median yields a lower
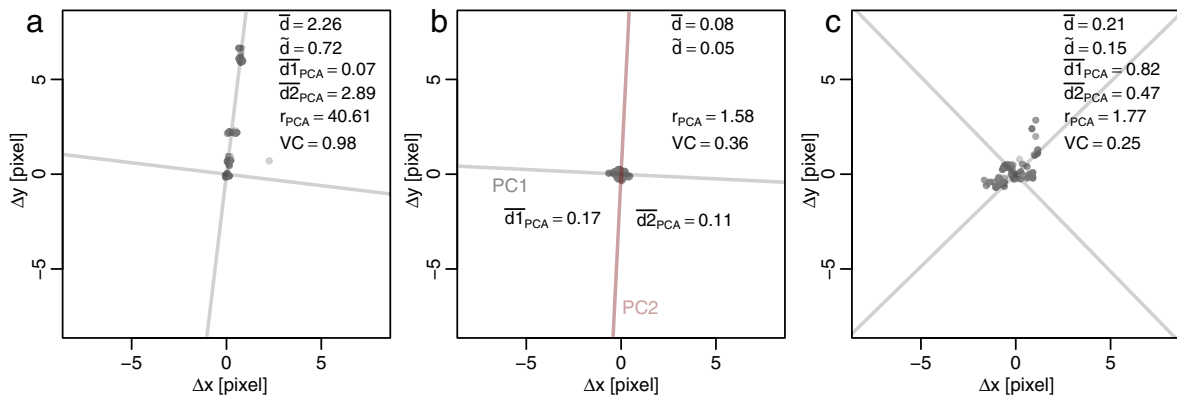
Fig. 2. Typical displacement vectors sampled from stack of displacement fields ($m = 18$) and a spatial neighborhood of 5×5 pixels. (a) Example of a landslide with a coherent displacement towards NNE. (b) Example of stable terrain with noisy measurements centered around zero. (c) Example of stable terrain with contradicting vectors pointing in the NE and SW directions. The proposed statistics and principal components are provided respectively illustrating their sensitivity under different conditions (see text for details).

estimate of the average displacement (Fig. 2a) when the sampled location was moving only for a short time period and most of the measurements show no displacement. For stable areas with measurement noise (Fig. 2b) or significant outliers (Fig. 2c), the median, however, better approximates the zero displacement.

2.2.3. Focal principal component analysis

Fig. 2c also provides an example for displacement measurements which point in different directions and are inconsistent with a landslide that maintains a coherent direction. Since simple averages cannot account for such cases, two additional indicators are proposed to quantify the coherence of the displacement direction over time. The first is based on the geometric interpretation of principal component analyses (PCA) as a best line-fit in a 2D space (Fig. 2). Given the matrix of eigenvectors Σ resulting from the PCA, a linear transform can be applied to project the displacement measurements along the first principal component ($PC1$) as denoted in Eq. (5).

$$D_{rot} = \Sigma D \tag{5}$$

No scaling and centering is used in the PCA so that this operation is essentially a rotation from $D = [\Delta X, \Delta Y]^T$ to $D_{rot} = [\Delta X_{rot}, \Delta Y_{rot}]^T$. In the rotated coordinate system, the measurements can be divided in two groups being $D_1 = \{D : \Delta X_{rot} > 0\}$ and $D_2 = \{D : \Delta X_{rot} < 0\}$. For each of those groups, the average displacements can be computed as in Eq. (3); the resulting means can be denoted as $\bar{d}_\rightarrow$ and $\bar{d}_\leftarrow$, respectively. A geometric interpretation of this operation is depicted in Fig. 2b. The second principal component ($PC2$) divides the 2D space into two half spaces and for each of those half spaces the mean displacement is computed. The ratio between the means in the two half spaces then provides a measure to quantify if the measurements point in similar directions or if they diverge in opposite directions. The ratio of the two means (f_{PCA}) is hence computed using Eq. (6).

$$f_{PCA} = \frac{\max\left(\bar{d}_\rightarrow, \bar{d}_\leftarrow\right)}{\min\left(\bar{d}_\rightarrow, \bar{d}_\leftarrow\right)} \tag{6}$$

Here the min and max operators are used to assure that $0 \leq f_{PCA} \leq +\infty$. If the average displacement magnitude in the two half spaces are equal, f_{PCA} will be zero, and $f_{PCA} \rightarrow +\infty$ as one of the two means dominates the other. Eq. (5) is not defined for $\min(\bar{d}_\rightarrow, \bar{d}_\leftarrow) = 0$ in which case f_{PCA} is defined as $+\infty$.
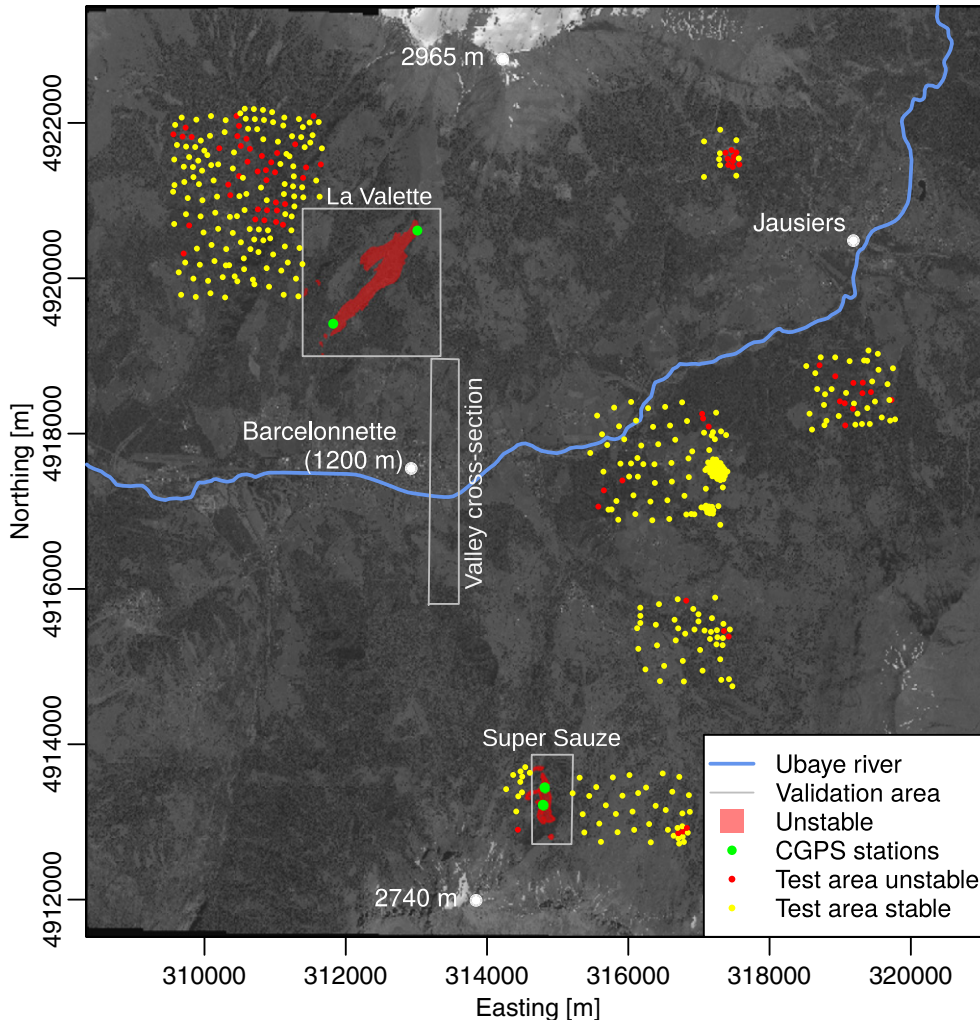
Fig. 3. Overview of the study site showing the footprints of all images used and the spatial locations of *validation areas* and *test areas*.

Table 2
Overview of the timing and geometry of the processed Pléiades satellite images. GSD is the ground sampling distance.

Satellite	Date	Time	Across track incidence angle	Along track incidence angle	Across track GSD	Along track GSD
PHR1A	2012-08-07	10:34:25	−7.06	5.79	0.72	0.71
PHR1A	2012-10-05	10:30:18	−4.02	12.28	0.74	0.71
PHR1A	2012-10-05	10:30:39	8.98	9.35	0.73	0.72
PHR1B	2013-07-31	10:30:51	−6.68	12.65	0.74	0.72
PHR1B	2013-07-31	10:31:26	14.39	7.84	0.74	0.74
PHR1B	2013-09-21	10:30:37	−5.07	12.88	0.74	0.71
PHR1B	2013-09-21	10:31:09	13.72	8.62	0.74	0.74
PHR1B	2014-06-20	10:37:39	−13.04	0.65	0.72	0.73
PHR1B	2014-06-20	10:38:21	11.42	−5.73	0.72	0.73

2.2.4. Vector coherence

A second measure (which relies on the vector direction, rather than on the magnitude) can be proposed considering the triangle equality which states that in the given 2D space $\|\Delta X + \Delta Y\| \leq \|\Delta X\| + \|\Delta Y\|$. This leads to a measure of the coherence of the vectors which is computed as in Eq. (7).

$$VC = \frac{\left\| \left(\sum_{i=1}^{|\Delta X|} \Delta X_i \right), \left(\sum_{i=1}^{|\Delta Y|} \Delta Y_i \right) \right\|}{\sum_{i=1}^{|\Delta X|} \| \Delta X_i, \Delta Y_i \|} \tag{7}$$

The vector coherence VC takes values in the interval [0,1] with $VC = 1$ if all displacement measurements are perfectly aligned in the same direction. This measure was also proposed in Dehecq et al. (2015) but not tested or exploited as a detector for surface displacement.

Among the four proposed indicators, $\bar{d}_{x,y,m,r}$ and $\tilde{d}_{x,y,m,r}$ rely on the persistence of the displacement magnitude in space and time, whereas f_{PCA} and VC take into account both direction and magnitude to quantify the coherence of the velocities in space and time. The effectiveness of those indicators to distinguish actual ground displacement from spurious detections in time-series is evaluated experimentally as described in Section 2.5.

2.3. Morphological and topographic filtering

By applying a simple threshold, any of the proposed indicators can be converted into a binary map which indicates areas with coherent and non-coherent displacement by 1 and 0, respectively. To further improve the binary detection map, three filters are applied which take into account the morphology, slope and orientation of the detected areas. As a first step, morphological filters (Serra, 1983) composed of a closing operation (disk structuring element with a radius of 10 pixels) and an opening operation (disk structuring element with a radius of 20 pixels) are applied. The main purpose of this step is to fill in small gaps in the detected areas and remove small isolated detections that resemble salt-and-pepper noise. All 8-connected neighboring pixels marked as 1 are then grouped into connected components. For each of the resulting patches the median slope angle θ is computed and all patches with $\theta < 15°$ are set to 0. This allows removal of multiple spurious detections that are located along the valley bottom and on agricultural areas with frequent strong changes of the surface appearance. For each of the remaining patches, the mean direction of the slope is computed (Wood, 1996) and compared to the mean direction of the detected displacements. If the difference among them exceeds $\frac{\pi}{5}$, the measurements are considered inconsistent with a mass movement that should follow the general slope direction. The specific thresholds were selected based on the analysis of the *validation areas* (Section 2.4.2) and in order to maximize the sum of user's and producer's accuracies.

2.4. Study site and data

The technique is used to investigate the landslide dynamics in the Ubaye valley (South French Alps); (Fig. 3) from 2012 to 2014. The area has a long-standing record of landslide activity including translational and rotational landslides as well as mudslides (Schlögel et al., 2015b). Recent studies have shown the potential of remote sensing to monitor individual slow-moving landslides in the valley using interferometric methods (Schlögel et al., 2015a), SAR pixel off-set tracking (Raucoules et al., 2013) and optical image correlation (Stumpf et al., 2014b) but did not address the automatic detection and monitoring of different landslides at the catchment scale. The rugged alpine terrain (1100–3000 m), the complex topography, and a forest cover of 40% render the site a challenging test case for the proposed methods and the use of image correlation techniques in general.
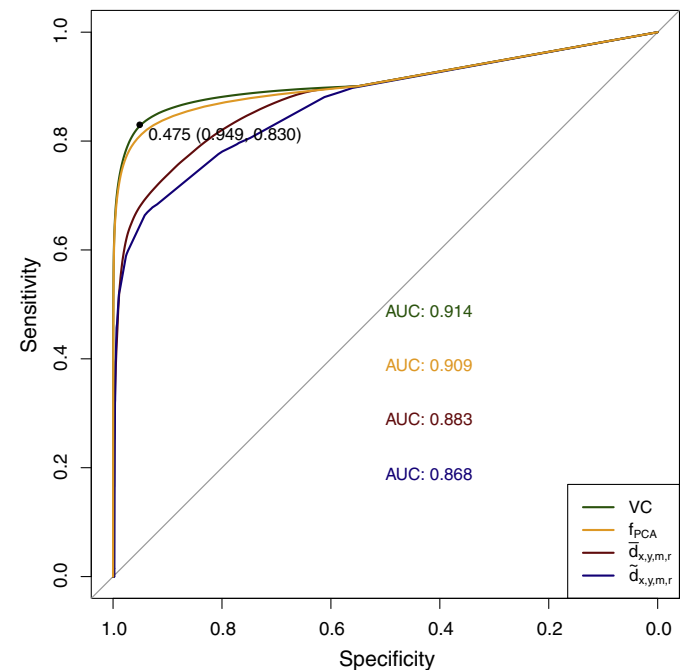
Fig. 4. ROC-based comparison of the tested spatio-temporal indicators ($r = 5, m = 18$). The *AUC* shows that vector-based indicators (VC and f_{PCA}) outperform indicators which consider the displacement magnitude ($\bar{d}_{x,y,m,r}$ and $\tilde{d}_{x,y,m,r}$). VC yields the best performance and a threshold of 0.475 maximizes the sum of sensitivity and specificity.
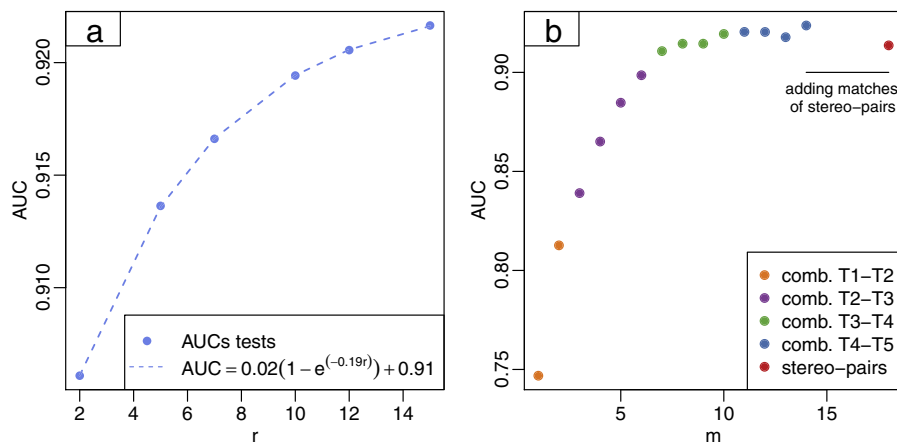
Fig. 5. Results of the sensitivity analysis. (a) The *AUC* using vector coherence (*V C*, $m = 18$) as a function of the considered neighborhood size *r*. The relationship is well approximated by a negative exponential fit suggesting an initial increase of the AUC and a saturation at larger neighborhood sizes. (b) The AUC using vector coherence (*V C*, $r = 5$) as a function of the number of available measurements *m*. The relationship shows the increasing robustness of the MPIC detection with increasing time-series length. The color code shows to which time-step the added displacement measurements belong. Adding matches among stereo-pairs rather decreases the performance.

2.4.1. Satellite image time series and pre-processing

A total of 9 Pléiades panchromatic images were acquired at 5 dates between August 2012 and June 2014 comprising 4 stereo-pairs and 1 monoscopic image with variable incidence angles and temporal baselines (Table 2).

Stumpf et al. (2014b) demonstrated that a precise co-registration and orthorectification can be achieved without ground control through a global bundle-adjustment of all images in one block and the use of the DSMs derived from the stereo-pairs for the orthorectification. Here we follow this processing strategy with the minor modification that the iterative bundle-adjustment is, in each iteration, re-initialized from the sensor model's rational polynomial coefficients (RPC) as specified in the image metadata. This avoids a bias accumulation in the absolute geolocation accuracy (see Supplementary Data - Fig. S1 for details) while retaining the benefits of a co-registration at sub-pixel precision. The bundle-adjustment resulted in a root-mean-squared error (*RMSE*) of 0.32 pixel in image geometry which quantifies the average co-registration quality among all images. From each of the 4 stereo-pairs, one respective DSM was generated at a pixel resolution of 0.5 m and each panchromatic image was orthorectified with the temporally closest DSM. The orthorectification was performed using a bicubic resampling scheme and the same grid for all orthoimages to assure the alignment of the pixel grid at a resolution of 0.5 m.

2.4.2. Reference data to assess the detection performance

To test the performance of the multi-temporal indicators (Section 2.2), two reference datasets were elaborated through the visual analysis of the orthoimages, the derived displacement fields and field surveys. Three areas in which recent landslide kinematics are well understood were selected as *validation areas* to compare the indicators and assess the sensitivity of the detection to the algorithm parameters. These areas comprise the La Valette landslide, the Super-Sauze landslide and a cross-section traversing the lower part of the Ubaye valley (Fig. 3). Considering all orthoimages, raw displacement fields, multiple field surveys, and CGPS (Continuous Global Positioning System) measurements (Section 2.4.3) these areas were classified into stable and unstable zones during the period August 2012 to June 2014. For an independent assessment of the detection accuracy an additional reference dataset was developed for several *test areas* depicted in Fig. 3. Considering that landslides typically cover only minor fractions of the landscape, a stratified sampling scheme was employed to obtain a sample which is representative for both

stable and unstable slopes. A total of 550 points were sampled in equal parts from two strata using non-aligned systematic sampling (Rosenfield et al., 1982) where one strata corresponded to slopes with at least one landslide activity between 1956 and 2009 (Schlögel et al., 2015b) and the second strata to slopes which remained stable during this period. The sampled point locations were visited during several field surveys to investigate signs of recent landslide activity and were marked as stable or unstable taking into account features such as fresh scarps and fractures, fresh polished surfaces and striations, disturbed drainage, no soil development, only fast growing and/or tilted vegetation, and considerable differences between form, roughness, texture and vegetation between slide and non-slide areas (Dikau, 1999). This analysis also included the visual interpretation of all available orthoimages and raw displacement fields to verify that measured displacement vectors are consistent with the slope morphology and surface texture, color, and shape depicted in the images. Following this analysis, 439 points were considered stable, 104 points unstable and 7 points were excluded since field visits and visual image interpretation remained inconclusive.

2.4.3. Continuous GPS measurements

Four dual-frequency CGPS receivers (Trimble NetR9 and NetRS) are installed at the La Valette and Super-Sauze landslides and are considered as reference sensors for the displacement field. The acquisition is performed daily at a frequency of 30 s for session durations of 24 h. The CGPS observations are processed using a PPP (Precise Point Positioning) approach which is a positioning method used to calculate precise positions using a single receiver from un-differenced phase measurements, precise clocks and precise satellite orbits. The positions time series are computed with the NRCan (Natural Resource Canada) PPP software (Malet et al., under review). For the CGPS located at La Valette and Super-Sauze landslides, the accuracy of the position is in the range of 5–8 mm horizontal and 8–13 mm in vertical.

2.4.4. Rainfall data

The Precipitation (P) data are hourly measurements of rain and snowfall (heated tipping bucket rain gauge) at Barcelonnette (1140 m, Météo-France station) which are summed for periods of 24 h (from 6 a.m. the first day to 5 a.m. the second day). The potential evapotranspiration (PET) is estimated daily with the Penmann-Monteith

equation from the minimum and maximum daily air temperature, the mean average wind velocity, the mean air's vapor content, the insolation time and the net radiation. The Effective Precipitation (EP) is then calculated as the daily difference P-PET, whereas negative EP values are set to zero. The EP is preferred here over P for two main reasons being, the time scale of the displacement measurements which capture only seasonal trends rather than short-term responses, and the fact that known slow-moving landslides in the area are primarily controlled by fluctuations in the ground-water table.

2.5. Experimental sensitivity analysis and accuracy assessment

Receiver operating characteristics (ROC) are used with the ground reference of the *validation areas* as the binary response variable to assess the detection performance of the four proposed indicators (Section 2.2) independently of any particular threshold (i.e. the threshold applied to produce a binary map for landslide occurrence). All possible thresholds on the respective indicator are tested, and for each possible threshold the respective resulting binary map is compared against the ground reference in the *validation areas*. The ROC curve is drawn in a 2-D space constituted by the *sensitivity* (or *true positive rate*) and the *specificity* (or *1-false positive rate*), and the area-under-the-curve (*AUC*) provides a global performance rating (Fawcett, 2006). The *AUC* is used to compare the performance
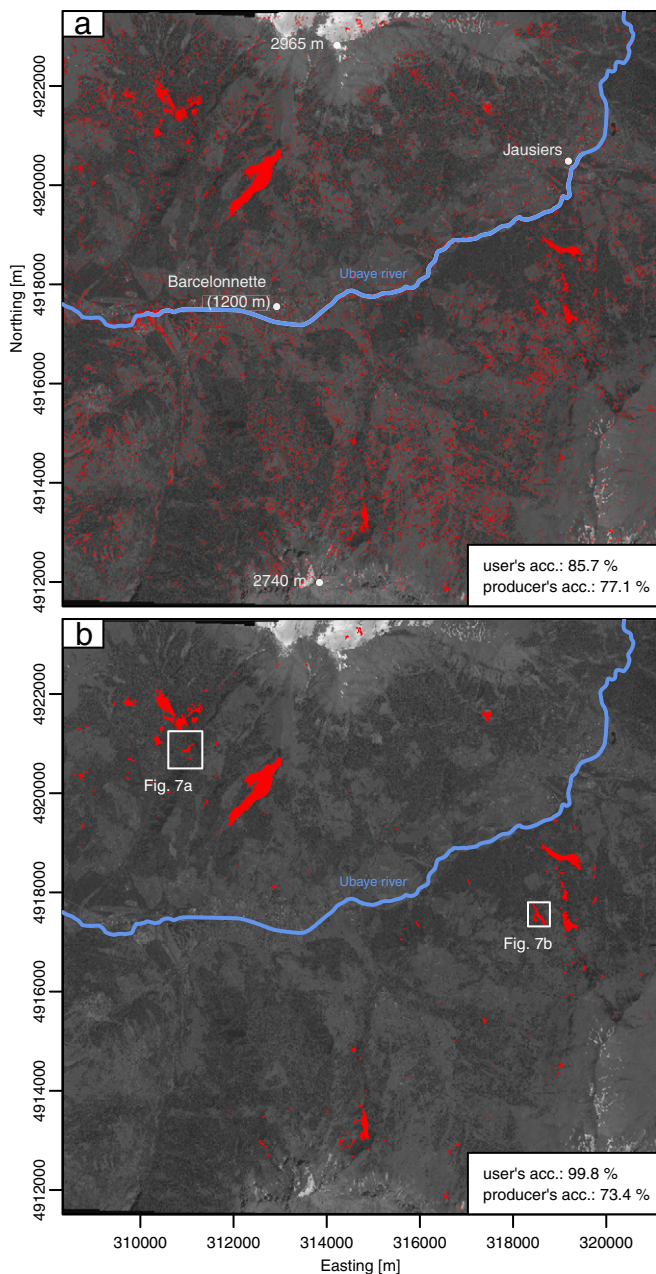
Fig. 6. Final landslide detection maps obtained with *VC*, $m = 14$, and $r = 10$ (a) before and (b) after morphological and topographic filtering.
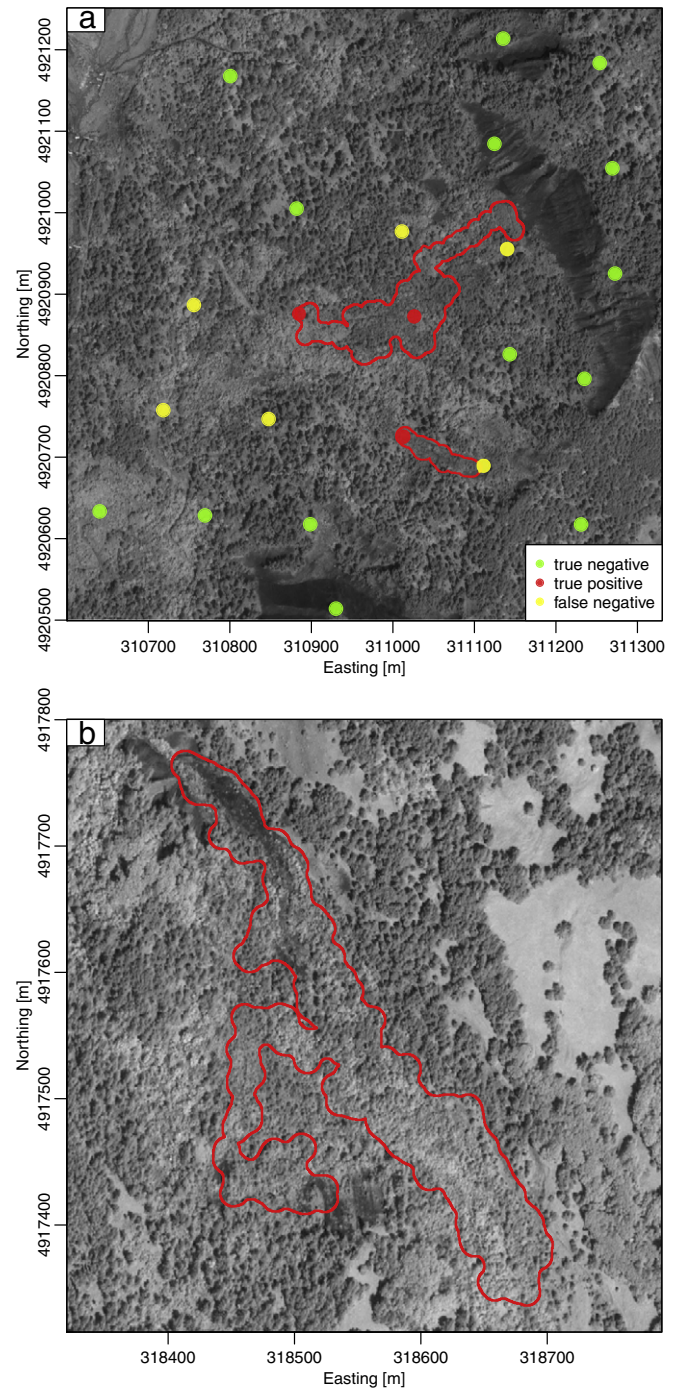
Fig. 7. Two subsets showing (a) an example for the non-detection of very slow displacement under dense vegetation, and (b) an example for the successful detection of a slow-moving landslide under dense vegetation.

of the four indicators and the impact of changes in the considered spatial neighborhood $r = \{2, 5, 7, 10, 12, 15\}$. In addition, it is important to consider that the length of the time-series and the number of available stereo-pairs may have a significant impact on the performance of the indicators derived through multi-temporal fusion. The vector of available images per time steps can be denoted as $K = \{1, 2, 2, 2, 2\}$ which according to Eq. (1) yields $m = 18$ measurements. To assess the effectiveness of the proposed MPIC scheme and the impact of limited data availability, m is reduced stepwise considering $m = \{18, 14, 13, 12, 11, \ldots, 1\}$ and the corresponding *AUC*s are computed each time. All ROC-based analyses are carried out using only the proposed indicators excluding subsequent morphological and topographic filtering. The best performing indicator is subsequently used to assess the user's and producer's accuracy (Story and Congalton, 1986) of the method against the ground reference developed for the *test areas*. This analysis includes the morphological and topographic filtering and thus provides an estimate of the accuracy of the complete processing chain. The measured displacement is assessed quantitatively against the permanent CGPS measurements.

3. Results and discussion

3.1. Sensitivity analysis

A ROC-based comparison of the multi-temporal indicators computed with $r = 5$ and the full time series ($m = 18$) is presented in Fig. 4. It illustrates that the indicators which are based on the coherence of the displacement vectors (VC and f_{PCA}) significantly outperform spatio-temporal averages of the displacement magnitude ($\bar{d}_{x,y,m,r}$ and $\tilde{d}_{x,y,m,r}$). Among the two vector-based indicators, VC provides a slightly higher sensitivity and was consequently used in all further experiments. With respect to the considered characteristics of landslide motion (coherent direction, spatial smoothness, temporal variability, Section 2.2), strategies taking into account both magnitude and direction of the motion are more robust. Simple averages of the magnitude, however, are rather sensitive to temporal and spatial gradients existing in the displacement fields.

Fig. 5a shows that the *AUC* generally increases if VC is computed based on larger spatial neighborhoods. This experimentally confirms the benefit of indicators which do not only consider the temporal information for each pixel in the stack but also information from neighboring pixels. The fitted negative exponential function suggests that the *AUC* increases are rather small beyond $r = 10$ and approach a maximum of $AUC = 0.93$.

The results of sensitivity analyses regarding the time-series length and the effectiveness of MPIC are presented in Fig. 5b. It shows that the *AUC* increases significantly from 0.75 to 0.94 with length of the time-series and the number of pair-wise matches added to the stack. The fact that the *AUC* increases not only when new dates are added but also through adding multiple matches among the same dates (points with identical color in Fig. 5b) confirms that the proposed MPIC matching scheme effectively improves the robustness of the detection. The increase of the detection accuracy is especially pronounced when moving from only 2 to about 10 combinations and slowly saturates towards 14 multi-temporal combinations. This indicates that, for the studied landslides, the proposed technique is already efficient with rather shorter time-series and few stereo-pairs, while the additional benefits from adding further dates might not outweigh the additional costs of data and computation. It is also notable that adding pair-wise matches among the orthoimages of the stereo-pairs rather reduces the performance. This is probably due to fact that the matching algorithm used for the stereo-reconstruction is similar to the MicMac correlator and will hence also produce similar errors in the same regions. The pair-wise matches among the orthoimages of the stereo-pairs were therefore excluded for further processing.

3.2. Accuracy assessment

To assess the overall accuracy of the detection after multi-temporal fusion and morphological-topographic filtering, 543 point locations in the *test areas* are considered (Fig. 3). The raw binary map resulting from an ROC-based thresholding (Fig. 4) of the vector coherence (VC, $r = 10$, $m = 14$) map is presented in Fig. 6a. While the raw output already provides an accuracy of $F = 0.81$, a significant amount of salt-and-pepper noise and false detections are still visible. The morphological-topographic filtering largely eliminates the salt-and-pepper noise and further improves the accuracy to $F = 0.85$, at the expense of a slight decrease in the producer's accuracy (Fig. 6b). All filtering steps contribute to the elimination of initial detections, whereas the morphological filtering step is in particular effective. While the applied slope threshold of $15°$ maybe still too rigorous for other sites with landslides on gentler slopes, the results also indicate that increased false detection rates with lower slope thresholds can be largely compensated with the subsequently applied aspect filter (Supplementary Data, Fig. S2c). Overall, these figures show that the combination of multi-temporal fusion and morphological-topographic filtering is effective to suppress nearly all spurious detections while retaining high sensitivity for real surface displacement. The few undetected landslide areas are mainly very slow moving parts of large landslides where dense vegetation omits reliable measurements of small displacements (Fig. 7a). While there are also counter examples where the proposed processing technique allows the detection of landslides with significant vegetation cover (Fig. 7b, Supplementary Data, Fig. S6d), small displacements under dense vegetation constitute an inherent limitation for the use of optical satellite data. Furthermore, it should be noted that the calculations based on spatial neighborhoods and morphological filtering (closing with a disk radius 20 pixels) impose limitations on the detectability of small or very elongated landslides.
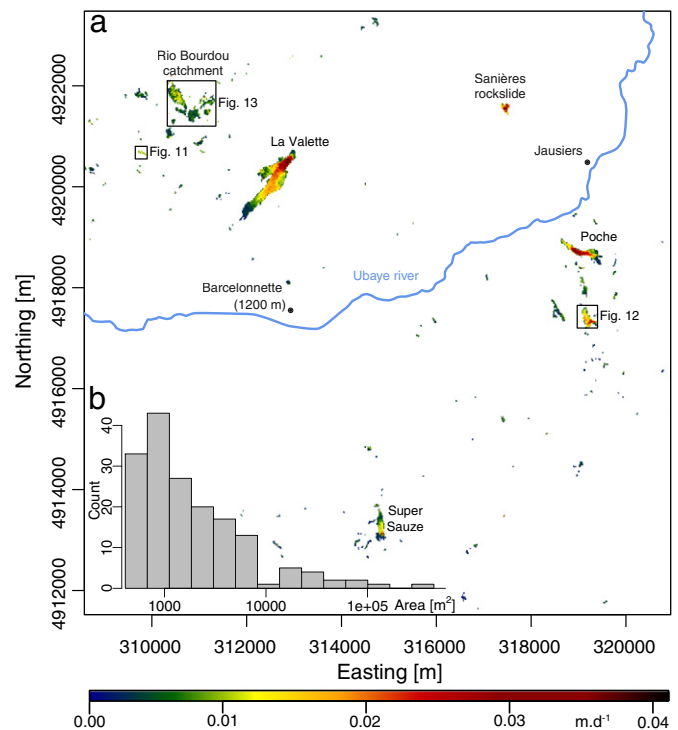
Fig. 8. (a) Average displacement rates [m·d^{-1}] of the detected landslides over the entire study period (2012/08/07–2014/06/20). (b) Histogram of the surface area of the detected landslides.

The 4 CGPS receivers at the La Valette (*LVA*1, *LVA*2) and the Super-Sauze landslides (*SAZ*1, *SAZ*2) allow to quantify the accuracy of the correlation-based velocity vectors. For this purpose the mean-absolute error (*MAE*) and the root-mean-squared errors (*RMSE*) are reported for both components of the horizontal displacement. To obtain the final displacement maps from a series of redundant measurements for each time step different strategies are possible. Given that orthorectification errors are proportional to the convergence angle, using the pairs with the smallest spatial baseline is a logical choice. Taking into account all reference measurements the misfit amounts to an $RMSE_{xy} = 0.36$ m ($RMSE_x = 0.14$ m and $RMSE_y = 0.33$ m). The distribution of the errors among the four stations is reported in greater detail in the Supplementary Data (Fig. S3). An

alternative strategy that takes into account all redundant measurements is to compute the mean displacement rates among all pair combinations of each time step. Greater robustness against outliers can also be obtained when considering in addition a small spatial neighborhood around the center of each CGPS station for the computation of the mean. The spatial neighborhood was set to a radius of 2.5 m to consider the area covered by the tripod of the CGPS receiver and closely adjacent pixels. The residual error when using this approach amounts to $RMSE_{xy} = 0.26$ m ($RMSE_x = 0.10$ m and $RMSE_y = 0.25$ m). The reduction of the $RMSE_{xy}$ by 74% shows the benefit of using stereo-pairs and averaging redundant measurements from all pair combinations covering a given time-step. The *RMSEs* for most measurements range between 0.04 and 0.13 m which is in line
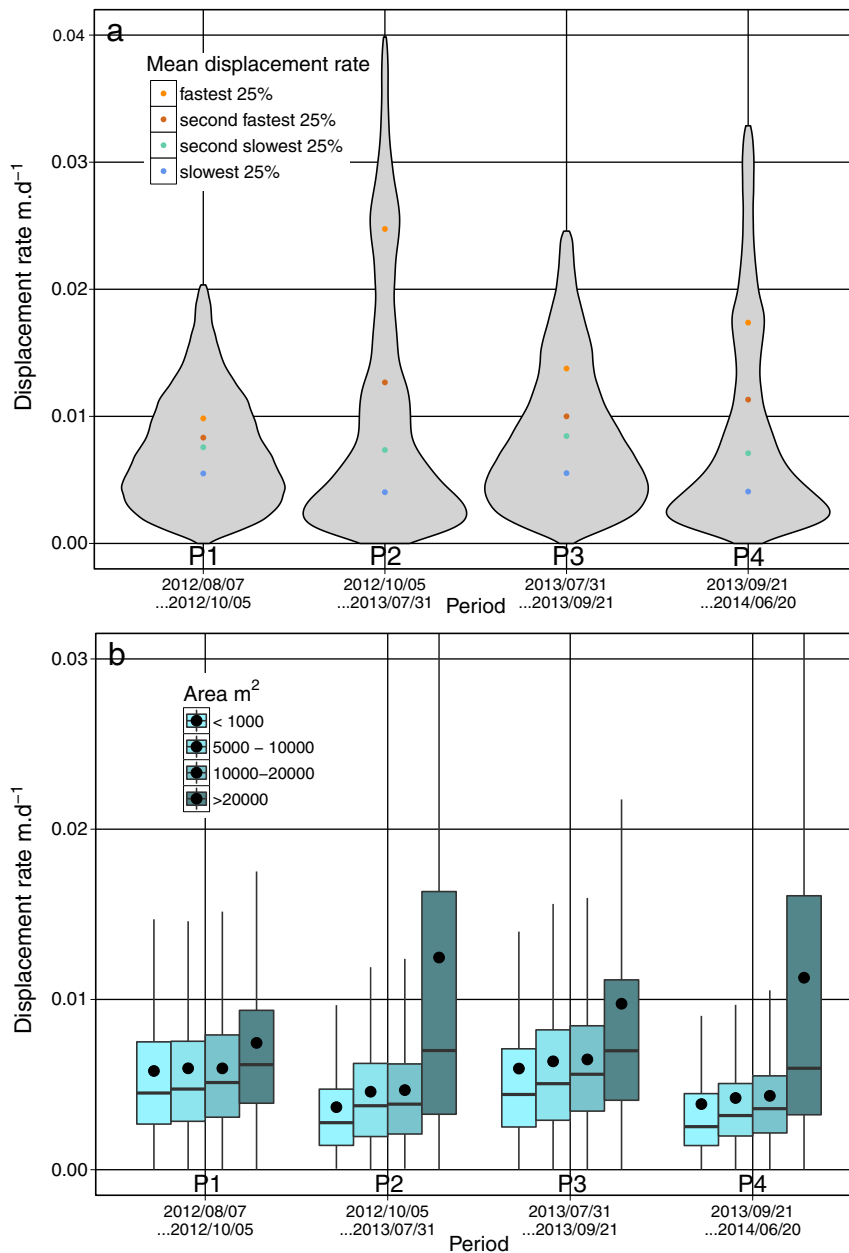
Fig. 9. (a) Probability distributions of the displacement rates of all detected pixels for the four observation periods and means per quartiles of the average displacement rate. The second and fourth periods show a characteristic tail towards higher displacement rates dominated by the fastest moving half of the pixels. (b) Boxplots of the displacements rates of all detected pixels grouped by landslide size and observation period showing a trend of faster displacement rates for landslide with larger surface areas. The groups comprise measurements from 71 (¡1000 m²), 69 (5000–10,000 m²), 19 (10,000–20,000 m²) and 10 landslides (¿20,000 m²), respectively.

with previous studies suggesting decimetric accuracies are feasible (Lacroix et al., 2015; Stumpf et al., 2014b). At two stations *LVA*1, *LVA*2, however, the $RMSE_y$ reaches up to 0.42 m. This appears to be related to higher residual errors in NS-direction observed during the bundle adjustment (Supplementary Data, Fig. S1) and could indicate higher-order geometric distortions which are not fully accounted with an affine refinement model.

3.3. Landslide kinematics and forcing conditions

After the ROC-based thresholding of VC and subsequent filtering a total of 169 active landslides are detected. An overview of their mean displacement rates and size distribution is given in Fig. 8. Besides the three largest landslides in the valley (La Valette, Super-Sauze, Poche) numerous landslides smaller than 10 , 000 m^2 are detected, most of which have not yet been registered in existing inventories for the period 1956–2009. Indeed Schlögel et al. (2015b) pointed out that the general difficulties in the mapping of small landslides with sparse image time-series lead to an underestimation of the lower area frequencies which would explain the observed discrepancy. At the same time it cannot be excluded that many of the detected smaller landslides have been activated only after 2009. The detected landslides concentrate in three spatial clusters located in the North-West (Riou-Bourdoux catchment), in the South (Sauze catchment) and in the East (Poche catchment). Most of the detections qualify as slow-moving flow-type landslides. The average displacement rates per pixel over all multi-temporal pairs for the entire study period range from 0.001 to 0.061 m·d^{-1}. The highest displacement rates of 0.17 m·d^{-1} were measured during the period 2013/07/31–2013 /09/21 on the Sanières rockslide which was triggered in early 2013.

A global analysis of the changes in the displacement rates of the detected landslides (i.e. all pixels which fall into the VC-based mask) for the four monitoring periods *P*1 (2012/08/07–2012 /10/05), *P*2 (2012/10/05–2013/07/31), *P*3 (2013/07/31–2013/09/21), and *P*4 (2013/09/21–2014/06/20) is presented in Fig. 9a. The distributions for the two periods that cover mainly autumn, winter and spring (*P*2 and *P*4) show long tails towards higher displacement rates

indicating an acceleration. Given that the number of available measurements depends on the surface area, it should be noted that those summary statistics are strongly dominated by larger landslides. Grouping all detected pixels according to the quartiles of their average displacement rate (2012/08/07–2014/06/20) also shows that mainly the fastest 50% of all pixels are accelerating during the periods *P*2 and *P*4. Fig. 9b presents the statistical distributions of all measurements on the detected landslides, when the measurements are grouped according to the surface area of the detected landslide they belong to. It shows that larger landslides tend to have higher average displacement rates and that the largest group (¿20 , 000 m^2) shows an acceleration during the periods *P*2 and *P*4 (Fig. 9b). To the best of our knowledge, a relationship between displacement rates and landslide extent has not been documented previously in the literature. While the roles of landslide material and slip surface geometry on the spatial variability of the displacement rates still require further investigation, the relationship could be explained by higher displacement rates contributing to a faster propagation of the landslide mass along the channel and thus to a greater extent. This seasonal pattern (acceleration during the periods *P*2 and *P*4) is similar to the one of the fastest 50% of all pixels (Fig. 9a). Surprisingly an inverse trend can be observed for medium size and small landslides ($<$20,000 m^2) which appear to feature slightly higher displacement rates during the summer month corresponding with the evolution of the slowest moving 50% of all detected pixels (Fig. 9a). The interpretation of this temporal pattern must, however, take into account the uncertainty of the measurement. The estimated $RMSE_{xy} = 0.26$ m propagates, due to different measurement intervals, unequally into the seasonal displacement rates (Supplementary Data, Fig. S5) and leads to apparently higher rates for the shorter summer periods (52 and 59 days). While several medium size and small landslides show clear signs of acceleration during the periods of *P*2 and *P*4 (e.g. Fig. 11), their summary statistics seem to be dominated by the measurement uncertainty. While these uncertainties hinder a further interpretation of the seasonal trends of very slow moving slope sections, it must be emphasized that they do not explain the acceleration of the fastest moving 50% during the two winter periods which is visible despite the bias towards higher summer displacement rates. Numerous previous studies have already demonstrated close links between seasonal rainfall patterns, groundwater flows and the kinematics of slow-moving landslides (Bennett et al., 2016; Handwerger et al., 2013; Hsu et al., 2014; Iverson and Major, 1987; Malet et al., 2005b; Reid, 1994; Zerathe et al., 2016). In the absence of comprehensive groundwater data for all detected landslides (only pore water pressure measurements for the La Valette and Super-Sauze landslides are available) we consider the mean effective precipitation (mm·d^{-1}) as a first order proxy for the hydrological conditions during each period. As demonstrated in Fig. 10, a close relationship exists between the seasonal pattern of the mean effective precipitation and the displacement rates of large landslides (20,000 m^2) and the fastest 50% of all detections. In this context, it should be mentioned that two seismic events occurred in the region on February 2012 (Mw 4.1) and April 2014 (Mw 4.9) leading to a peak ground acceleration (PGA) of up to 60 cm·s^{-2} (Courboulex et al., 2014). While Lacroix et al. (2015) observed an acceleration of slow-moving landslides at a comparable PGA, the CGPS measurements on the La Valette and Super-Sauze landslides, do not show any change of the displacement rates in response to the seismic events. This supports the view that the change in the hydrological conditions is the main driver of the acceleration during the periods *P*2 and *P*4. Further analyses of interdependencies among factors such as landslide material, slip surface geometry and water flow paths would be necessary to better understand the spatial pattern of the surface motion (e.g. Handwerger et al., 2015; Krzeminska et al., 2013; Malet et al., 2005b; Van Asch et al., 2007). In the absence of sufficient background data for most of the observed landslides, however, we limit the remainder of the

Fig. 10. Relationship between the evolution of the cumulative and mean effective precipitation and the changes of the mean displacement rates of the two fastest moving quartiles of all pixels, and landslides with a surface area 20,000 m^2. The similar evolution suggests a strong control of seasonal hydrological conditions on the motion of large landslides and the faster 50% of the detected slope sections.

discussion to a qualitative analysis of displacement fields for some exemplary landslide complexes.

The landslide complex presented in Fig. 12 features a strong acceleration during the autumn-winter-spring periods P2 and P4 with displacement rates of up to 0.064 m·d^{-1} between September 2013 and June 2014 (Fig. 12d).

In particular the southern (upslope) section is covered by dense vegetation (Supplementary Data, Fig. S6b) which could not have developed if such high displacement rates had persisted over longer time spans. This indicates that the observed acceleration significantly exceeds the long-term average. The displacement fields for the summer months show low displacement rates except for the period P3 during which the south-eastern section (activated during the period P2) remains active. The displacement in this zone persists also during period P4 but is partially masked due to strong surface changes and thus temporary decorrelation (Fig. 12d). Decorrelation also occurs at

a steep secondary scarp in the central part of the landslide which, due to a lack of coherent measurements, is excluded during the detection phase. Fig. 13 displays the headwaters of the Riou-Bourdoux catchment where an acceleration during the periods P2 and P4 is visible (Fig. 13b, d). In particular the south-western landslide (Les Aiguettes) shows a clear acceleration with a consistent spatial pattern during those periods with higher average effective rainfall. While previous studies that relied on detailed tree ring analysis and visual analysis of orthophotographs have shown no activity for the years 2004–2010 (Saez et al., 2013), the correlation-based displacement measurements clearly indicate a reactivation of the landslide complex with displacement rates of up to 0.03 m·d^{-1}. The very high resolution of the derived displacement field allows to identify a stable zone within the center of the landslide which corresponds to an in-situ crest of the underlying stable bedrock. During the summer month (Fig. 13a, c) the landslide complex shows very limited
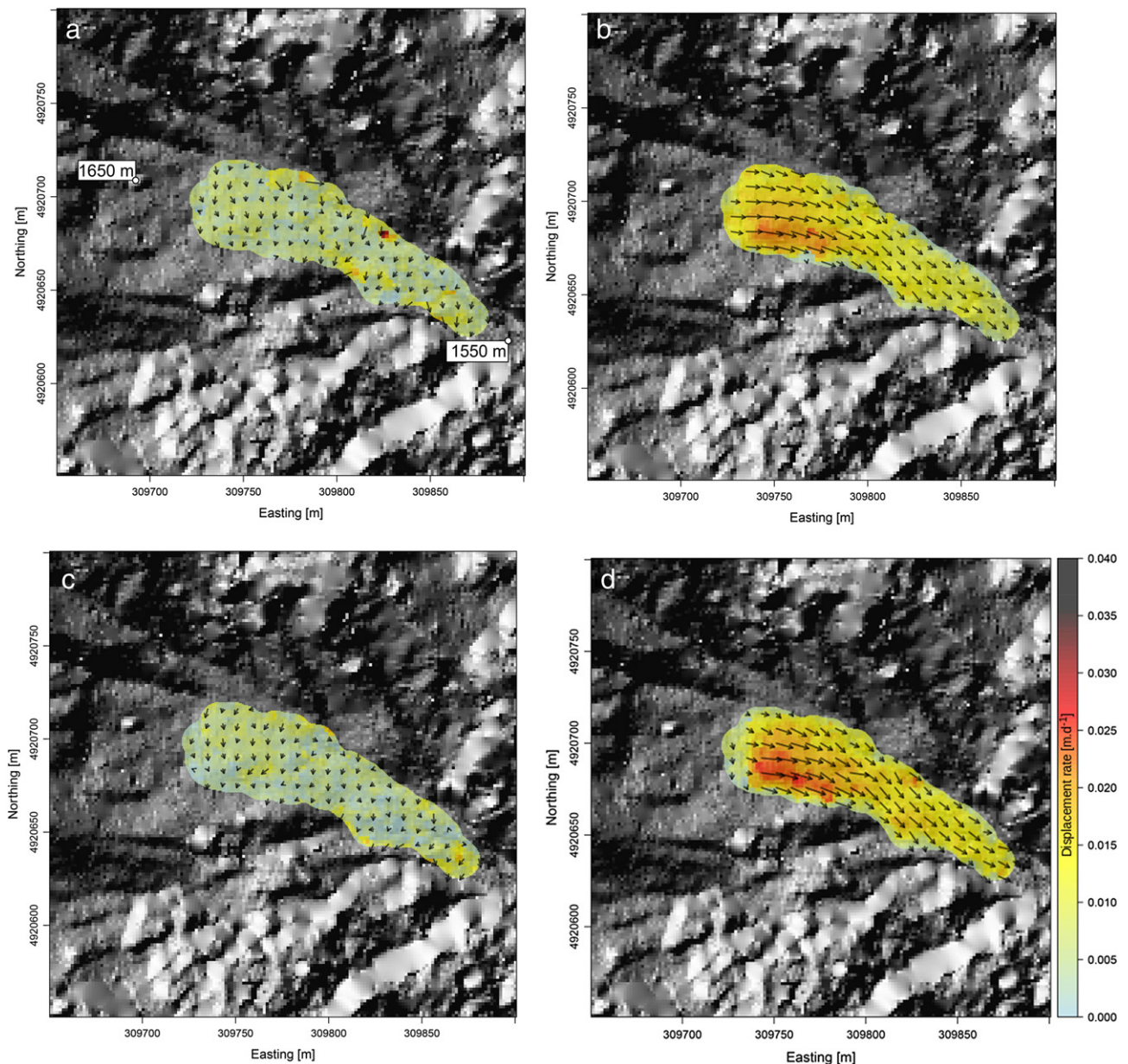
Fig. 11. Series of displacement rate maps [m·d^{-1}] for a small landslide in the Riou-Bourdoux catchment for the monitoring periods (a) P1, (b) P2, (c) P3, and (d) P4.

activity. A zone of higher summer velocities that can be noted in the north-western corner is likely an artefact resulting from dense vegetation and steep slope at the scarp of the landslide. These zones were, nevertheless, detected since the winter velocities were sufficiently high and coherent to outweigh the co-registration noise.

4. Conclusion

This study targeted the development and testing of a new method for the detection and monitoring of slow-moving landslides through the correlation-based analysis of optical SITS. The developed MPIC processing scheme is developed and tested with a sequence of multi-temporal Pléiades monoscopic and stereoscopic images, and applied to investigate a landslide-prone landscape in the South French Alps.

Among four tested indicators for the spatio-temporal persistence of the displacement measurements, the vector coherence VC is found to be the most robust. A sensitivity analysis regarding the length of the time-series shows, that even with a limited number of dates, the MPIC scheme greatly improves the detection accuracy. Further accuracy gains are achieved through the consideration of larger spatial neighborhoods in the computation of the vector coherence. The particular window size, however, depends on the respective applications case and should take into account the expected spatial smoothness of the displacement field and the size of the searched features. A detection based on VC allows to considerably reduce the number of false detections while still retaining a high sensitivity with a producer's accuracy of 77%. A sequence of morphological and topographic filters further eliminates nearly all false detections while a producer's accuracy of >73% is preserved. The technique, in
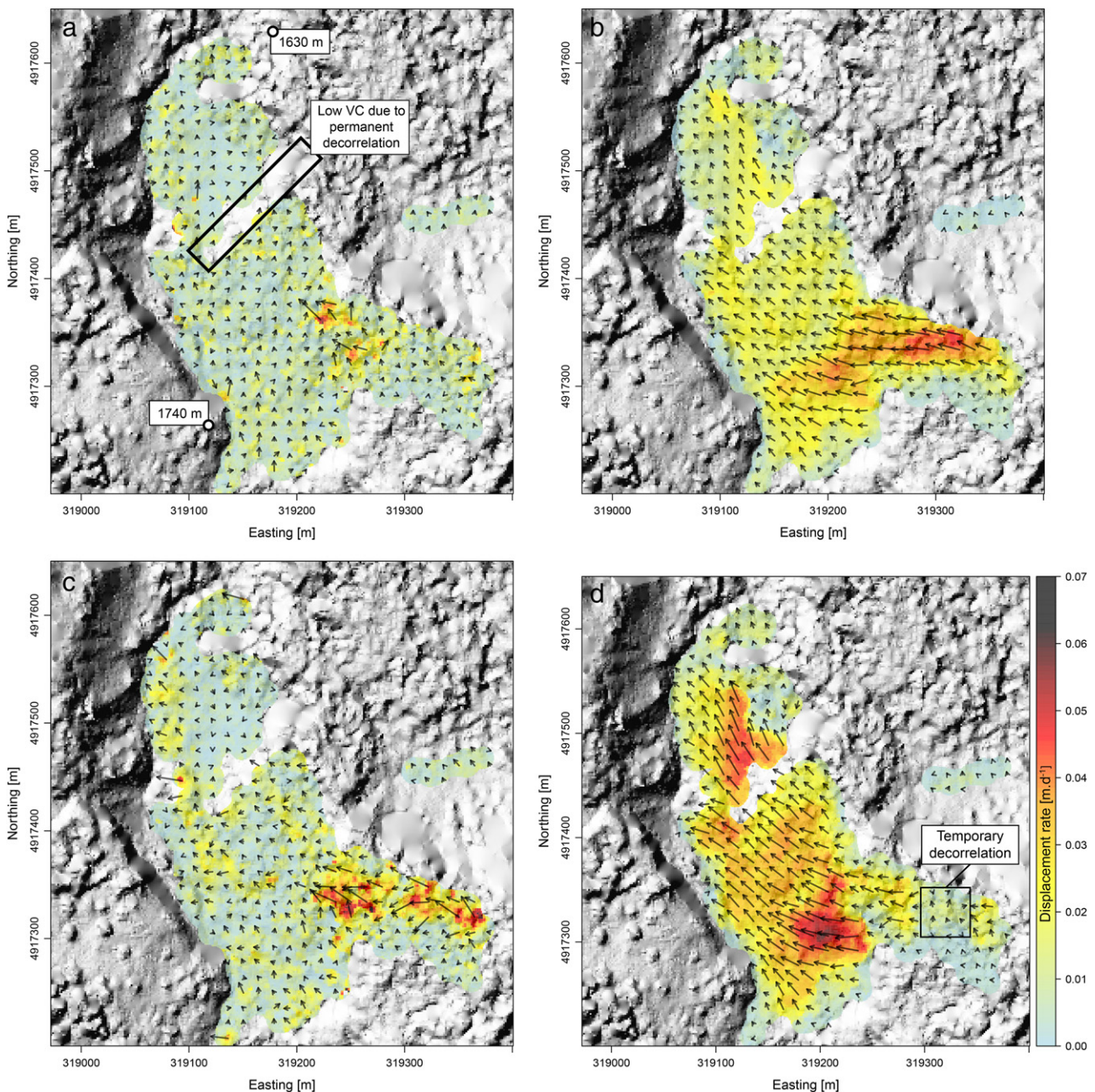
Fig. 12. Series of displacement rate maps [m • d^{-1}] for a landslide complex located south of the Poche landslide for the monitoring periods (a) *P1*, (b) *P2*, (c) *P3*, and (d) *P4*.
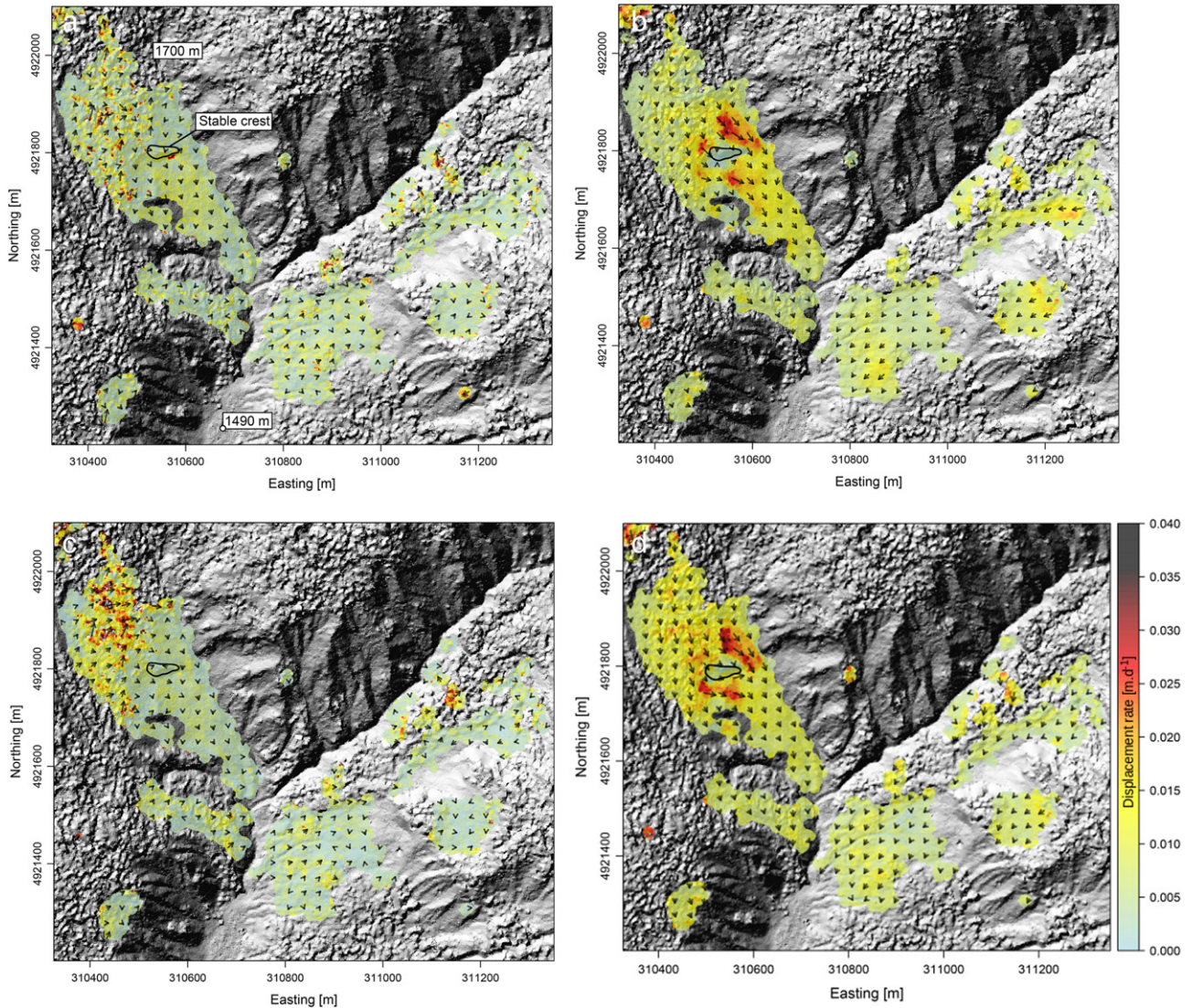
Fig. 13. Series of displacement rate maps [m·d^{-1}] for a large landslide complex in the Riou-Bourdoux catchment for the monitoring periods (a) *P1*, (b) *P2*, (c) *P3*, and (d) *P4*.

many cases, detects movement under significant vegetation cover, whereas false negatives can still arise in areas with very slow movement (<1.6 m·yr^{-1}) and dense vegetation cover. An assessment of the derived displacement fields at the location of dual-frequency CGPS measurements shows that averaging measured velocities from all pairs covering a given time-step (i.e. when stereo-pairs are available for at least one date) reduces $RMSE_{xy}$ by about 74% to an $RMSE_{xy} = 0.26$ m. The averaging enables to reduce the measurement variance, whereas the remaining $RMSE_{xy}$ is dominated by a residual bias in the north-south component. Further research should address the elimination of this geometric bias which is likely the result of higher order terms that are not properly addressed with an affine error model during bundle adjustment. The derived motion fields provide a detailed view into the spatio-temporal dynamics of numerous slow-moving landslides in the investigated catchment, many of which were previously unrecorded or could only be surveyed at specific points and very irregular time intervals. A joint analysis of the derived multi-temporal motion fields shows a close relationship between the seasonal averages of the effective precipitation and the displacement rates of larger, slow-moving landslides. The proposed technique opens new perspectives in the operational exploitation of

optical SITS for a more accurate detection and monitoring of slow-moving landslides over wide areas. The current implementation relies on high-performance infrastructure and parallel processing and is undergoing active development to allow an efficient processing of SITS from Sentinel-2, Landsat-8 and similar satellite platforms on ESA's cloud-based processing infrastructure (ESA, 2016). While this could enable an effective background monitoring with a dense temporal sampling of seasonal dynamics further improvements of the measurement accuracy are still required to account for the coarser spatial resolution. This may include inversion strategies (e.g. Casu et al., 2011) and the estimation of higher order residuals in the co-registration based on measurements over stable terrain.

Acknowledgments

Appendix A. Supplementary data

Supplementary data to this article can be found online at http://dx.doi.org/10.1016/j.rse.2016.11.007.

References

Behling, R., Roessner, S., Golovko, D., Kleinschmit, B., 2016. Derivation of long-term spatiotemporal landslide activity — multi-sensor time series approach. Remote Sens. Environ. 186, 88–104.

Behling, R., Roessner, S., Kaufmann, H., Kleinschmit, B., 2014. Automated spatiotemporal landslide mapping over large areas using rapideye time series data. Remote Sens. 6 (9), 8026–8055.

Bennett, G.L., Roering, J.J., Mackey, B.H., Handwerger, A.L., Schmidt, D.A., Guillod, B.P., 2016. Historic drought puts the brakes on earthflows in northern California. Geophys. Res. Lett. 43 (11), 5725–5731.

Berthier, E., Vadon, H., Baratoux, D., Arnaud, Y., Vincent, C., Feigl, K.L., Remy, F., Legresy, B., 2005. Surface motion of mountain glaciers derived from satellite optical imagery. Remote Sens. Environ. 95 (1), 14–28.

Casson, B., Delacourt, C., Allemand, P., 2005. Contribution of multi-temporal remote sensing images to characterize landslide slip surface? Application to the La Clapière landslide (France). Nat. Hazards Earth Syst. Sci. 5 (3), 425–437.

Casu, F., Manconi, A., Pepe, A., Lanari, R., 2011. Deformation time-series generation in areas characterized by large displacement dynamics: the SAR amplitude pixel-offset SBAS technique. IEEE Trans. Geosci. Remote Sens. 49 (7), 2752–2763.

Courboulex, F., Delouis, B., Dujardin, A., Deschamps, A., Bertrand, E., Causse, M., Maron, C., Sira, C., Cultrera, G., 2014. The two events of Barcelonnette (French Alps), 2012 (mw 4.1) and 2014 (mw 4.9): the role of directivity on ground motions, macroseismic intensities and site effects. Second European Conference on Earthquake Engineering and Seismology, Istanbul. pp. 1–3.

Cruden, D.M., Varnes, D.J., 1996. Landslide Types and Processes. In: Landslides Investigation and Mitigation. No. Special Report 247 in Transportation Research Board, US National Research Council. Turner, A.K. and Schuster, R.L., pp. 36–75.

Debella-Gilo, M., Kääb, A., 2011. Sub-pixel precision image matching for measuring surface displacements on mass movements using normalized cross-correlation. Remote Sens. Environ. 115 (1), 130–142.

Dehecq, A., Gourmelen, N., Trouve, E., 2015. Deriving large-scale glacier velocities from a complete satellite archive: application to the Pamir–Karakoram–Himalaya. Remote Sens. Environ. 162, 55–66.

Delacourt, C., Allemand, P., Casson, B., Vadon, H., 2004. Velocity field of the "La Clapiére landslide measured by the correlation of aerial and QuickBird satellite images. Geophys. Res. Lett. 31 (15).

Dikau, R., 1999. The Recognition of Landslides. Springer Berlin Heidelberg, Berlin, Heidelberg, pp. 39–44.

ESA, 2016. Geohazards TEP.

Fahnestock, M., Scambos, T., Moon, T., Gardner, A., Haran, T., Klinger, M., 2016. Rapid large-area mapping of ice flow using Landsat 8. Remote Sens. Environ. 185, 84–94. November.

Fawcett, T., 2006. An introduction to ROC analysis. Pattern Recogn. Lett. 27 (8), 861–874.

Guzzetti, F., Mondini, A.C., Cardinali, M., Fiorucci, F., Santangelo, M., Chang, K.-T., 2012. Landslide inventory maps: new tools for an old problem. Earth-Sci. Rev. 112 (1), 42–66.

Handwerger, A.L., Roering, J.J., Schmidt, D.A., 2013. Controls on the seasonal deformation of slow-moving landslides. Earth Planet. Sci. Lett. 377, 239–247.

Handwerger, A.L., Roering, J.J., Schmidt, D.A., Rempel, A.W., 2015. Kinematics of earthflows in the northern California coast ranges using satellite interferometry. Geomorphology 246, 321–333.

Heid, T., Kääb, A., 2012. Evaluation of existing image matching methods for deriving glacier surface displacements globally from optical satellite imagery. Remote Sens. Environ. 118, 339–355.

Hooper, A., Bekaert, D., Spaans, K., Arıkan, M., 2012. Recent advances in sar interferometry time series analysis for measuring crustal deformation. Tectonophysics 514, 1–13.

Hsu, Y.-J., Chen, R.-F., Lin, C.-W., Chen, H.-Y., Yu, S.-B., 2014. Seasonal, long-term, and short-term deformation in the central range of Taiwan induced by landslides. Geology 42 (11), 991–994.

Iverson, R.M., Major, J.J., 1987. Rainfall, ground-water flow, and seasonal movement at minor creek landslide, northwestern California: physical interpretation of empirical relations. Geol. Soc. Am. Bull. 99 (4), 579–594.

Joyce, K.E., Samsonov, S., Manville, V., Jongens, R., Graettinger, A., Cronin, S.J., 2009. Remote sensing data types and techniques for lahar path detection: a case study at Mt. Ruapehu, New Zealand. Remote Sens. Environ. 113 (8), 1778–1786.

Krzeminska, D., Bogaard, T., Malet, J.-P., Van Beek, L., 2013. A model of hydrological and mechanical feedbacks of preferential fissure flow in a slow-moving landslide. Hydrol. Earth Syst. Sci. 17 (3), 947–959.

Kurtz, C., Stumpf, A., Malet, J.-P., Gançarski, P., Puissant, A., Passat, N., 2014. Hierarchical extraction of landslides from multiresolution remotely sensed optical images. ISPRS J. Photogramm. Remote Sens. 87, 122–136.

Kääb, A., 2005. Combination of SRTM3 and repeat ASTER data for deriving alpine glacier flow velocities in the Bhutan Himalaya. Remote Sens. Environ. 94 (4), 463–474.

Lacroix, P., Berthier, E., Maquerhua, E.T., 2015. Earthquake-driven acceleration of slow-moving landslides in the Colca valley, Peru, detected from Pléiades images. Remote Sens. Environ. 165, 148–158.

Lauknes, T., Shanker, A.P., Dehls, J., Zebker, H., Henderson, I., Larsen, Y., 2010. Detailed rockslide mapping in northern Norway with small baseline and persistent scatterer interferometric sar time series methods. Remote Sens. Environ. 114 (9), 2097–2109.

Lebegue, L., Greslou, D., de Lussy, F., Fourest, S., Blanchet, G., Latry, C., Lachérade, L., Delvit, J.M., Kubik, P., Déchoz, C., 2012. PLEIADES-HR image quality commissioning. ISPRS-Int. Arch. Photogramm. Remote. Sens. Spat. Inf. Sci. 1, 561–566.

Leprince, S., Barbot, S., Ayoub, F., Avouac, J.-P., 2007. Automatic and precise orthorectification, coregistration, and subpixel correlation of satellite images, application to ground deformation measurements. IEEE Trans. Geosci. Remote Sens. 45 (6), 1529–1558.

Leprince, S., Berthier, E., Ayoub, F., Delacourt, C., Avouac, J.-P., 2008. Monitoring earth surface dynamics with optical imagery. Eos 89 (1), 1–2.

Li, Z., Shi, W., Myint, S.W., Lu, P., Wang, Q., 2016. Semi-automated landslide inventory mapping from bitemporal aerial photographs using change detection and level set method. Remote Sens. Environ. 175, 215–230.

Lu, P., Stumpf, A., Kerle, N., Casagli, N., 2011. Object-oriented change detection for landslide rapid mapping. IEEE Geosci. Remote Sens. Lett. 8 (4), 701–705.

Mackey, B.H., Roering, J.J., 2011. Sediment yield, spatial characteristics, and the long-term evolution of active earthflows determined from airborne lidar and historical aerial photographs, Eel River, California. Geol. Soc. Am. Bull. 123 (7-8), 1560–1576.

Malet, J.-P., Boetzle, P., Masson, F., Desprez, A., Ferhat, G., Ulrich, P. Evaluation of different processing strategies of continuous gps (CGPS) observations for landslide monitoring. J. Geod. 20, (under review).

Malet, J.-P., Van Asch, T.W., Van Beek, R., Maquaire, O., 2005. Forecasting the behaviour of complex landslides with a spatially distributed hydrological model. Nat. Hazards Earth Syst. Sci. 5 (1), 71–85.

Malet, J.-P., Van Asch, T.W., Van Beek, R., Maquaire, O., 2005. Forecasting the behaviour of complex landslides with a spatially distributed hydrological model. Nat. Hazards Earth Syst. Sci. 5 (1), 71–85.

Mansour, M.F., Morgenstern, N.R., Martin, C.D., 2011. Expected damage from displacement of slow-moving slides. Landslides 8 (1), 117–131.

Martha, T.R., Kerle, N., Jetten, V., van Westen, C.J., Kumar, K.V., 2010. Characterising spectral, spatial and morphometric properties of landslides for semi-automatic detection using object-oriented methods. Geomorphology 116 (1), 24–36.

Martha, T.R., Kerle, N., van Westen, C.J., Jetten, V., Kumar, K.V., 2012. Object-oriented analysis of multi-temporal panchromatic images for creation of historical landslide inventories. ISPRS J. Photogramm. Remote Sens. 67, 105–119.

Mondini, A., Guzzetti, F., Reichenbach, P., Rossi, M., Cardinali, M., Ardizzone, F., 2011. Semi-automatic recognition and mapping of rainfall induced shallow landslides using optical satellite images. Remote Sens. Environ. 115 (7), 1743–1757.

Petley, D., 2012. Global patterns of loss of life from landslides. Geology 40 (10), 927–930.

Pierrot-Deseilligny, M., Deveau, M., Belvaux, J., Choqueux, G., Maillet, G., Girod, L., Rupnik, E., Muller, J., 2015. MicMac, Apero, Pastis and Other Beverages in a Nutshell!, October 23, 2015 Edition. Marne-la-Vallée. Oct

Quincey, D.J., Braun, M., Glasser, N.F., Bishop, M.P., Hewitt, K., Luckman, A., 2011. Karakoram glacier surge dynamics. Geophys. Res. Lett. 38 (18).

Raucoules, D., De Michele, M., Malet, J.-P., Ulrich, P., 2013. Time-variable 3d ground displacements from high-resolution synthetic aperture radar (SAR). Application to La Valette landslide (South French Alps). Remote Sens. Environ. 139, 198–204.

Reid, M.E., 1994. A pore-pressure diffusion model for estimating landslide-inducing rainfall. J. Geol. 709–717.

Rosenau, R., Scheinert, M., Dietrich, R., 2015. A processing system to monitor greenland outlet glacier velocity variations at decadal and seasonal time scales utilizing the Landsat imagery. Remote Sens. Environ. 169, 1–19.

Rosenfield, G.H., Fitzpatrick-Lins, K., Ling, H.S., 1982. Sampling for thematic map accuracy testing. Photogramm. Eng. Remote. Sens. 48, 131–137.

Rosu, A.-M., Pierrot-Deseilligny, M., Delorme, A., Binet, R., Klinger, Y., 2015. Measurement of ground displacement from optical satellite image correlation using the free open-source software MicMac. ISPRS J. Photogramm. Remote Sens. 100, 48–59.

Saez, J.L., Corona, C., Stoffel, M., Berger, F., 2013. High-resolution fingerprints of past landsliding and spatially explicit, probabilistic assessment of future reactivations: Aiguettes landslide, southeastern French Alps. Tectonophysics 602, 355–369.

Scherler, D., Leprince, S., Strecker, M.R., 2008. Glacier-surface velocities in alpine terrain from optical satellite imagery–accuracy improvement and quality assessment. Remote Sens. Environ. 112 (10), 3806–3819.

Schlögel, R., Doubre, C., Malet, J.-P., Masson, F., 2015a. Landslide deformation monitoring with ALOS/PALSAR imagery: a D-InSAR geomorphological interpretation method. Geomorphology 231, 314–330.

Schlögel, R., Malet, J.-P., Remaître, A., Reichenbach, P., Doubre, C., 2015b. Analysis of a landslide multi-date inventory in a complex mountain landscape: the Ubaye valley case study. Nat. Hazards Earth Syst. Sci. Discuss. 3 (3), 2051–2098.

Serra, J., 1983. Image Analysis and Mathematical Morphology. Academic Press, Inc.

Story, M., Congalton, R.G., 1986. Accuracy assessment-a user˅'s perspective. Photogramm. Eng. Remote. Sens. 52 (3), 397–399.

Stumpf, A., Kerle, N., 2011. Object-oriented mapping of landslides using random forests. Remote Sens. Environ. 115 (10), 2564–2577.

Stumpf, A., Lachiche, N., Malet, J.-P., Kerle, N., Puissant, A., 2014a. Active learning in the spatial domain for remote sensing image classification. IEEE Trans. Geosci. Remote Sens. 52 (5), 2492–2507.

Stumpf, A., Malet, J.-P., Allemand, P., Ulrich, P., 2014b. Surface reconstruction and landslide displacement measurements with Pléiades satellite images. ISPRS J. Photogramm. Remote Sens. 95, 1–12.

Stumpf, A., Malet, J.-P., Puissant, A., Travelletti, J., 2016. Monitoring of earth surface motion and geomorphologic processes by optical image correlation. In: Baghdadi, N., Zribi, M. (Eds.), Land Surface Remote Sensing: Environment and Risks. vol. 6. ISTE, Elsevier., pp. 147–190.

Van Asch, T.W., Van Beek, L., Bogaard, T., 2007. Problems in predicting the mobility of slow-moving landslides. Eng. Geol. 91 (1), 46–55.

Wasowski, J., Bovenga, F., 2014. Investigating landslides and unstable slopes with satellite multi temporal interferometry: current issues and future perspectives. Eng. Geol. 174, 103–138.

Wood, J., 1996. The Geomorphological Characterisation of Digital Elevation Models. (Ph.D. thesis). Department of Geography, University of Leicester, Leicester, UK.

Yamaguchi, Y., Tanaka, S., Odajima, T., Kamai, T., Tsuchida, S., 2003. Detection of a landslide movement as geometric misregistration in image matching of SPOT HRV data of two different dates. Int. J. Remote Sens. 24 (18), 3523–3534.

Zerathe, S., Lacroix, P., Jongmans, D., Marino, J., Taipe, E., Wathelet, M., Pari, W., Smoll, L.F., Norabuena, E., Guillier, B., et al. 2016. Morphology, structure and kinematics of a rainfall controlled slow-moving Andean landslide, Peru. Earth Surf. Process. Landf.

Zhao, C., Lu, Z., Zhang, Q., de La Fuente, J., 2012. Large-area landslide detection and monitoring with alos/palsar imagery data over northern California and southern Oregon, USA. Remote Sens. Environ. 124, 348–359.